communications materials

A Nature Portfolio journal

Article

Article in Press

https://doi.org/10.1038/s43246-026-01346-z

Embedded multilayer strain architectures create self-sensing multifunctional titanium in additive manufacturing

Alisha Bhatt[1,2,3,4] ✉, Wenqing Chen[1,3,4], Zheng Wu[5], Prasenjit Kabi[1,3,4], Paul Brennan[3,6], Samy Hocine[1,2], Elena Ruckh[1,2], Hazel Assender[5], Rob Snell[7], Ian Todd[7], Peter D. Lee[1,2] ✉ & Manish K. Tiwari[1,3,4] ✉

Multifunctional structural metals capable of monitoring their internal mechanical state are increasingly important for aerospace, biomedical, and intelligent manufacturing applications, yet integrating thermally sensitive sensing architectures into high-temperature metal additive manufacturing remains challenging. Here we show that multilayer strain sensing architectures can be embedded directly within Ti-6Al-4V during laser powder bed fusion by combining high-resolution printing of polymer–metal gauges with powder mediated thermal protection. We evaluate four sensor architectures, including commercial foil gauges and directly printed gauges with different dielectric layers, and identify material stacks that survive embedding while retaining electrical functionality. The embedded sensors preserve strain sensing performance under mechanical loading, maintain structural integrity, and exhibit cytocompatibility. These results establish a route to multifunctional titanium with internal sensing capability and provide a materials integration framework for embedding functional devices within additively manufactured metals.

Metal components capable of internally monitoring strain are increasingly important for applications in aerospace structures[1], biomedical implants[2,3], and structural health monitoring systems[4]. Conventional monitoring approaches rely on external sensors, which provide limited spatial resolution and cannot capture stress distributions within the material[5,6]. Embedding sensors directly during metal additive manufacturing (AM) offers a pathway to measure strain internally and in real time, enabling predictive maintenance and integration with digital twin frameworks in critical engineering systems[7,8]. Titanium alloys such as Ti-6Al-4V are widely used in biomedical[9] and aerospace components[10] because of their high mechanical strength, corrosion resistance, and biocompatibility[11]. However, integrating sensors within these alloys remains challenging because of their high melting temperature[12], low thermal conductivity, and the sensitivity of polymer dielectric materials[13] to localized laser heating during fabrication.

Previous strategies for incorporating sensors in metallic structures include protective coating, cavity integration, or the use of prefabricated metallic sensing layers[14,15]. Although these approaches have shown promise, they often increase fabrication complexity, restrict design flexibility[16–18], and have primarily been demonstrated in alloys such as stainless steel 316L[19,20] or Inconel 718[21]. Commercial strain gauges typically consist of metallic foils mounted on polymer dielectric substrates, and their integration into titanium alloy components during laser powder bed fusion (LPBF) remains difficult[22]. The extreme thermal gradients and rapid heating cycles associated with LPBF can lead to polymer degradation, delamination, or loss of electrical functionality, limiting the reliability of embedded sensing systems[23].

Direct ink writing (DIW) provides a route to deposit functional materials with high spatial precision and flexible sensor geometries[24]. Tripropylene glycol diacrylate (TPGDA) was selected as the dielectric layer because it can form uniform thin films compatible with roll-to-roll deposition (R2R)[25], provides sufficient thermal stability under controlled curing conditions, and promotes adhesion with metallic nanoparticle inks used for strain sensing[26]. Multilayer sensor architectures, where dielectric and conductive layers are independently optimized, can improve both resolution and durability under the thermal cycling conditions associated with LPBF processing[23,27,28]. The combination of DIW printing and TPGDA

[1]Department of Mechanical Engineering, University College London, Torrington Place, London, UK. [2]Research Complex at Harwell, Harwell Science & Innovation Campus, Didcot, UK. [3]Nanoengineered Systems Laboratory, University College London, Torrington Place, London, UK. [4]UCL Hawkes Institute, University College London, London, UK. [5]Department of Materials, University of Oxford, Parks Road, Oxfordshire, Oxford, UK. [6]Department of Electronic and Electrical Engineering, University College London, Torrington Place, London, UK. [7]Department of Materials and Engineering, University of Sheffield, Western Bank, Sheffield, UK. ✉e-mail: abhatt@anl.gov; peter.lee@ucl.ac.uk; m.tiwari@ucl.ac.uk

dielectric layers therefore enables the fabrication of multilayer polymer–metal strain gauges compatible with metal AM.

Here we present a strategy for embedding multilayer strain-sensing architectures within Ti-6Al-4V components fabricated by LPBF. A powder-mediated shielding layer is used to mitigate thermal exposure during laser processing, while DIW enables direct deposition of polymer–metal sensing structures. The embedded sensors retain strain-sensing functionality under mechanical loading and exhibit cytocompatibility. These results establish a materials integration framework for embedding functional devices within additively manufactured metals, enabling the development of self-monitoring structural components for aerospace, biomedical, and intelligent manufacturing applications. Powder-mediated shielding strategies in LPBF have previously been reported to reduce thermal exposure of sensitive features during processing[29,30]. In contrast to these studies, the present work integrates this concept with roll-to-roll processed dielectric layers, direct ink writing of strain gauges, and in-process embedding within Ti-6Al-4V components, alongside post-fabrication evaluation of electrical performance and biocompatibility.

Results and discussion

Surface roughness and wettability of tripropylene glycol diacrylate (TPGDA)

We selected TPGDA as a model dielectric to establish a transferable strategy for integrating printable polymer layers within metal substrates. TPGDA provides a processable thin film compatible with R2R deposition, enabling controlled investigation of surface modification and printing behavior relevant to a broader class of printable dielectrics. Importantly, the purpose of this study was to demonstrate a proof of concept for surface treatment and printing optimization; therefore, the methodology and findings are expected to be transferable to other printable dielectric materials with a similar processing requirement. In this multilayer system, the dielectric surface governs both ink wettability and interfacial stability and is therefore critical for achieving high-resolution patterning and mechanical durability. The strain gauge comprises a Ti-6Al-4V base layer, a TPGDA dielectric layer, and a sensing layer formed from commercial *50 wt. %* silver nanoparticle dispersion in tripropylene glycol mono methyl ether (TPM) ink, hence the surface morphology of the dielectric is critical for both printability and durability. The TPGDA dielectric layer was deposited on Ti-6Al-4V using the R2R vacuum web coating facility.

Atomic force microscopy (AFM) imaging (Fig. 1a) shows that TPGDA deposition preserves the underlying substrate roughness, but the as-deposited surface exhibits insufficient wettability for DIW[31]. Therefore, plasma and electron beam irradiation (EBI) treatments were applied to modify the TPGDA surface and improve its printability. Increasing the plasma current enhanced surface etching and produced pronounced peaks, whereas EBI generated a more symmetrical distribution of valleys and peaks, resulting in a smoother and more uniform surface morphology. Increasing the plasma current enhanced etching and produced peaks, whereas EBI generated a more symmetrical distribution of valleys and peaks, yielding a smoother and more uniform surface. Quantitative roughness parameters (Fig. 1b) confirmed that both EBI and low-current plasma yielded lower surface roughness (S_a) and root mean square (*RMS*) values in comparison to the higher plasma, suggesting their suitability for DIW.

Spectroscopic analysis confirmed these observations. Fourier Transform Infrared spectroscopy (FTIR) spectra (Fig. 1c) showed an increase in the intensity of the ester carbonyl (C = O) stretching band at ~1730 cm^{-1} with increasing plasma current, indicating enhanced surface polarity and wettability. This band is characteristic of the acrylate groups present in TPGDA and its polymerized network. The increase in C = O intensity is interpreted as evidence of increased surface oxidation/polar functionality following plasma treatment, which can enhance the surface polarity of the cured polymer coating and improve wettability for subsequently deposited layers, such as TPM silver nanoparticle ink. It should be noted that this interpretation relates to the surface properties of the cured polymer coating rather than the initial wetting of the monomer on the substrate prior to curing. In addition, the FTIR peak at approximately 810 cm^{-1}, corresponding to the out-of-plane bending of the acrylate C = C bond, is commonly used to assess the amount of residual unsaturation and therefore the degree of cure of the coating. A reduction in the intensity of this peak indicates a greater extent of polymerization. Similarly, EBI modified the surface chemistry of the TPGDA layer, increasing surface polarity and correlating with the observed reduction in infrared (IR) transmittance. Both plasma and EBI improved the surface energy and promoted ink adhesion. However, increasing plasma current also increased surface roughness, which can negatively affect high-resolution printing.

The practical consequence of these effects was captured by TPM silver nanoparticle ink contact angle measurements (Fig. 1d). Low-current plasma produced moderate spreading and stable contact angles, while high-current plasma and EBI induced extensive spreading and very low contact angles due to the combined effects of polarity and morphology. Excessive wettability, however, led to ink bleeding and compromised printing resolution (Supplementary Fig. 2). Overall, low-current plasma treatment achieved the optimal balance of smooth morphology, sufficient polarity, and controlled wettability, enabling both reliable adhesion and high-resolution strain gauge patterning. These results establish that controlled tuning of dielectric surface chemistry and morphology is essential for integrating conductive features within multilayer architectures and provide a generalizable framework for printable polymer–metal interfaces in AM environments. Surface smoothing is required during the DIW deposition stage to ensure uniform ink wetting and continuous conductive filament formation. Although the strain gauges are subsequently embedded within an LPBF-fabricated cavity, surface topography at the deposition stage governs feature definition, ink continuity, and electrical percolation prior to embedding

Thermal constraints of the dielectric layer define curing conditions for nanoparticle strain gauges

We establish the thermal constraints governing integration for the polymer dialectic and conductive ink within the LPBF environment (see Supplementary Fig. 3 for the methodology). Thermogravimetric analysis (TGA) revealed progressive weight loss beginning at ~220 °C, indicative of polymer degradation (Fig. 2a). Differential scanning calorimetry (DSC) analysis further identifies a glass transition at ~260 °C, crystallization at ~280 °C, and complete melting at ~350 °C (Fig. 2b). Together these results define a narrow thermal processing window, in which exposure temperatures above ~200 °C leads to irreversible damage and change in the polymer network.

We then examine the curing behavior of the TPM silver nanoparticle ink under these constraints, droplets were deposited onto plasma-treated TPGDA films and furnace-cured between 100–250 °C (Fig. 2ci–ii). Resistance decreased linearly with curing time across all conditions, with faster reduction at higher temperatures due to enhanced conductivity (Fig. 2d). However, temperatures ≥200 °C induce microstructural degradation characterized by pore formation within the conductive layer (Fig. 2e). This behavior is consistent with accelerated solvent evaporation and reduced mechanical robustness. The maximum thermal tolerance of the ink was ~250 °C for 8500 s before degradation was evident.

While elevated temperatures promote rapid conductivity development, they also approach the degradation threshold of both the dielectric and conductive layers. We therefore identified curing at 150 °C for 3800 s, which produced strain gauges with ~350 Ω resistance comparable to commercial devices[32–35], while avoiding degradation of both the dielectric and the conductive layer.

These results establish the additional requirements for a protective powder layer during laser scanning and a carefully controlled curing protocol to ensure device stability and performance. These results motivate the incorporation of a powder-mediated shielding strategy to mitigate transient thermal exposure, enabling retention of both dielectric integrity and conductive functionality during embedding.

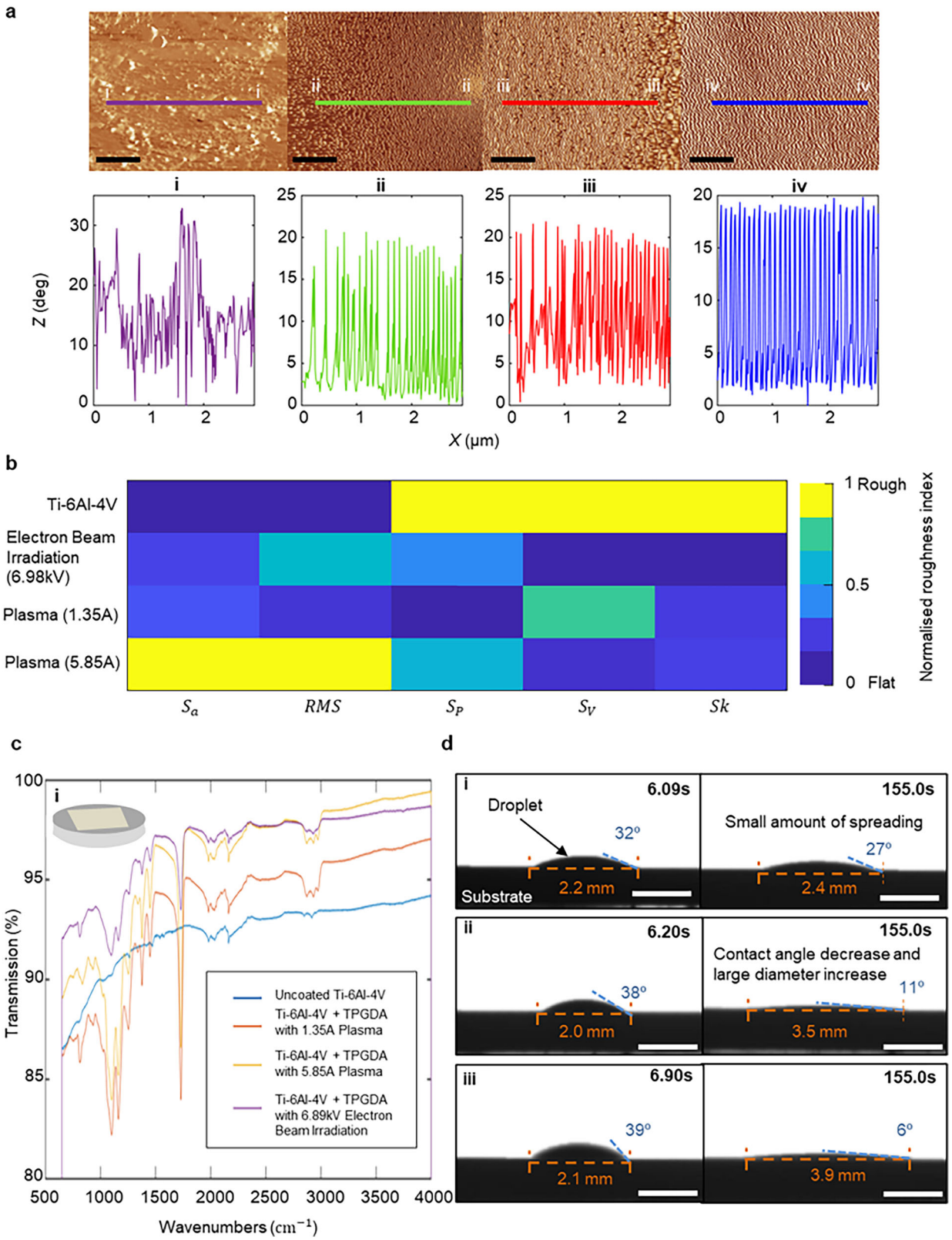

High-resolution strain gauge embedding via printing and thermal management strategies

Embedding high-resolution strain gauges into LPBF-fabricated Ti-6Al-4V parts requires careful coordination of printing precision, thermal management, and material selection. The process begins with the micropipette nozzle, where tip geometry directly affects printing fidelity. Figure 3ai–iii shows the nozzle tip end pulled by the P-1000 micropipette puller (P-1000), demonstrating that the pull velocity influences the final tip size. Figure 3bi–iii shows the tip end where the heating temperature is indirectly defined as the ramp temperature, which is not the real temperature. Using the P-1000 puller, we found that decreasing the ramp temperature and pull velocity produced smaller, more reproducible tips, whereas higher pull

Fig. 1 | a Atomic force microscopy (AFM) images of substrates (Supplementary Fig. 1). **ai** Uncoated additive manufactured (AM) Ti-6AI-4V, **aii** for tripropylene glycol diacrylate (TPGDA), plasma treated at 1.35 A, **aiii** TPGDA plasma treated at 5.85 A, and **aiv** TPGDA electron beam irradiation (EBI) treated at 6.98 kV. All scale bars correspond to 1 µm. **b** A normalized colourmap showing varying roughness parameters (S_a: average top-skin roughness, *RMS*: root mean square average, S_p: maximum profile peak height, S_v: maximum profile valley height and *Sk*: skewness) for four different surfaces including uncoated AM Ti-6AI-4V, for TPGDA plasma treated at 1.35 A, TPGDA plasma treated at 5.85 A and TPGDA EBI treated at 6.98 kV. The values are normalized by column ($X_{normalization} = \frac{(X_i - X_{minimum})}{(X_{maximum} - X_{minimum})}$, where X_i: the actual value, $X_{minimum}$: minimum value on the row and $X_{maximum}$: maximum value in the row (Supplementary Tables 2–4)[45]. **c** Fourier-transform infrared spectroscopy (FTIR) for different surface-treated TPGDA. **ci** Schematic of the sample on the Ti-6AI-4V sample, which has a thin coating of coated (TPGDA). **d** Contact angle and diameter measurements, where a droplet of 50 wt. % dispersion in tripropylene glycol mono methyl ether (TPM) silver nanoparticle ink was dropped on Ti-6AI-4V-coated TPGDA for the three different surface treatments, which were analyzed. Goniometer time-series images capturing the evolution of a droplet from when the droplet hits the surface and droplet morphology after 155 s for **di–ii** plasma treatment of 1.35 A, **di–ii** plasma treatment of 5.85 A, and **di–ii** EBI of 6.98 kV. All the scale bars are 1 mm.

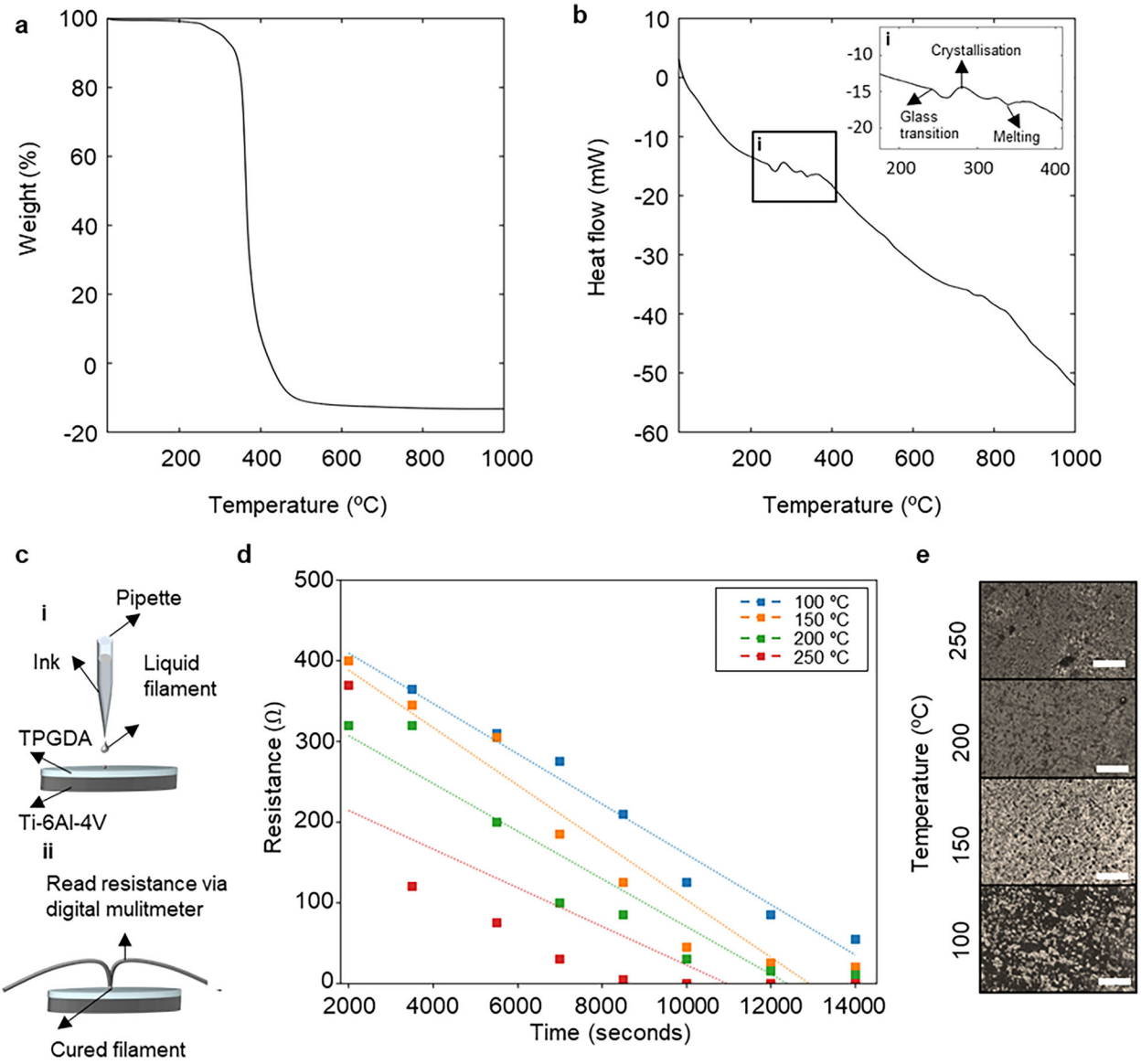

Fig. 2 | a Thermogravimetric analysis (TGA) profile and **b** differential scanning calorimetry (DSC) for tripropylene glycol diacrylate (TPGDA). **bi** Shows a subsection highlighter by (**b**), where the black box shows an endothermic dip and exothermic peak. **ci–ii** Schematic where a droplet of 50 wt. % dispersion in tripropylene glycol mono methyl ether (TPM) silver nanoparticle ink on Ti-6Al-4V-coated TPGDA treated with plasma coating at 1.35 A was cured under four different temperatures (100, 150, 200 and 250 °C). **d** Scatter plot of the resistance against time for four different curing temperatures. **e** Optical images of the four different times. All the scale bars are 600 µm.

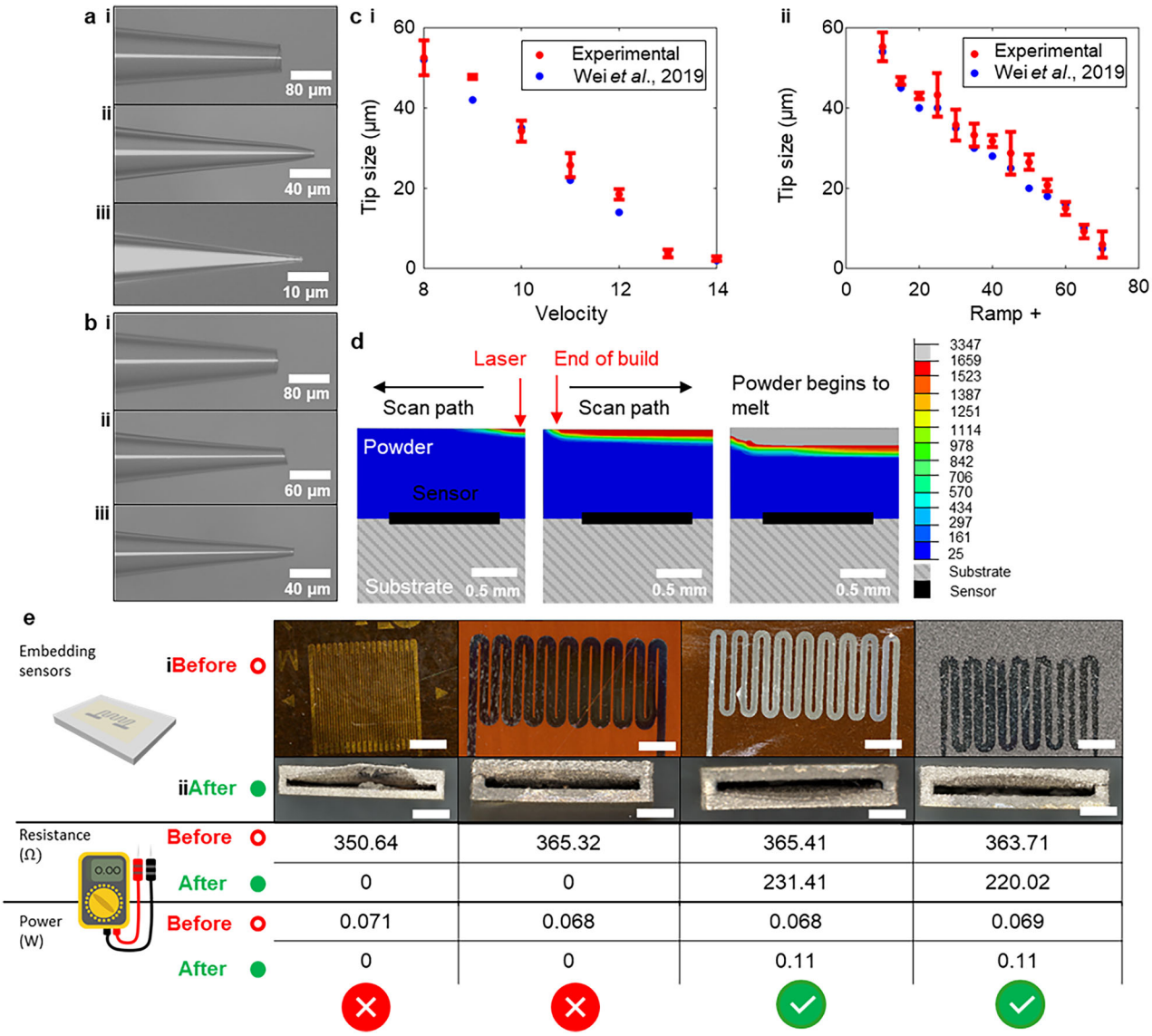

Fig. 3 | a Optical imaging of the tip ends, showing the effect of the pulling velocity. Here, the value stands for the scale unit of the puller it is related to the pulling velocity, but not the real value of pulling velocity, where **ai** 8 Ramp, **aii** 12, and **aiii** 14. **b** Optical imaging of the tip ends, showing the effect of the Ramp. Here, the value stands for the scale unit of the puller it is related to the heating temperature, but not the real value of temperature, where **bi** +10 Ramp, **bii** +40 Ramp, and **biii** 70+ Ramp. **ci–ii** Plot showing velocity dependence of the tip ending tip size of glass capillary pulled by micropipette puller compared to ref. 36. **d** Plot showing temperature dependence of the tip ending size of the glass capillary pulled by the micropipette puller compared to ref. 36. **d** A schematic representation of the relative position of the X-ray beam shows the melt pool shape and heat-affected zone for a protective layer of 1 mm (Supplementary Tables 6, 7, and 8 show the parameters used for the FEA simulation). Temperature in Celsius. **e** Optical images of four different sensors, which include a commercial foil strain gauge with a polyamide film (PI) backing; a direct ink write (DIW) printed strain gauge with 50 wt. % dispersion in tripropylene glycol monomethyl ether (TPM) silver nanoparticle ink with a PI backing; DIW-printed strain gauge with 50 wt. % dispersion in TPM silver nanoparticle ink with glass fiber (GF) reinforced phenolic backing; and a Ti-6AI-4V base layer, tripropylene glycol diacrylate (TPGDA) backing, and a sensor layer printed with 50 wt. % dispersion in TPM silver nanoparticle ink in respective order. **e** Is before embedding, and **eii** is after the embedding. Scale bars are 20 μm for **ei** and 0.25 mm for **eii**. The resistance, R (Ω) and power P (W) of the four strain gauges were recorded before embedding and after. **c**, **d** Data points represent the mean tip size obtained from ten measurements, and error bars represent the standard deviation of these measurements.

velocities increased the tip size due to extended neck reshaping (Fig. 3ci–ii). Tip size variation remained below 5% across all conditions, consistent with ref. 36, ensuring both high spatial resolution (≤10 μm) and nozzle durability required for reliable conductive ink deposition. Nozzle tip breakage and bleeding were observed at low pull velocities (of 14). Based on these results, a ramp of 65 + and a pull velocity of 12 were selected to achieve a durable, high-resolution nozzle (Supplementary Fig. 4).

The printing process is followed by embedding under LPBF conditions, where thermal exposure can compromise strain gauge integrity. A 1 mm layer of Ti-6Al-4V powder was applied over the gauges to act as a thermal barrier. Simulations indicate that, although surface powder temperatures reach ~3347 °C during laser scanning, the thermal effect near the embedded gauges is reduced to ~25 °C, effectively mitigating thermal degradation (Fig. 3d). Although the thermal simulation presented indicated that a thinner powder layer could reduce the peak temperature at the strain gauge, a 1 mm layer was selected to ensure a sufficient safety margin and account for any discrepancies in powder spreading and potential laser exposure. This protective layer also alleviates stress concentrations at the embedding site, helping preserve gauge structure and function. The thermal model represents transient heat conduction during the laser scanning process. A first-

order estimate of the thermal penetration depth is obtained using $L \approx \sqrt{\alpha\tau}$[37], where α is the thermal diffusivity of the powder and τ is the laser interaction time. Using the process parameters ($v = 1.2$ m/s, see Supplementary Methods), the estimated penetration depth is on the order of ~10 μm, which is significantly smaller than the 1 mm powder protective layer. This analytical estimate is consistent with the FEM results, which show a minimal rise in temperature at the location of the sensor. The selected 1 mm powder layer will provide a substantial additional safety margin to ensure sensor protection against any potential local thermal fluctuations during the laser scanning process. Although the thermal model predicts that the bulk temperature at the sensor location remains close to ambient (~25 °C), this value represents the average temperature within the powder-shielded region and does not account for localized thermal excursions or thermo-mechanical stresses at polymer-adhesive metal interfaces. Consequently, failure of the PI-backed gauges is considered likely to be associated with interfacial degradation arising from thermal cycling and thermal expansion mismatch rather than excessive bulk heating of the sensor itself. The Ti-6Al-4V powder layer used for thermal shielding during LPBF experiences a thermal gradient in which regions may undergo full melting, partial sintering, or remain unmelted depending on proximity to the melt pool. Following completion of the AM build and powder removal, the final component forms a dense Ti-6Al-4V structure with gages on interior surfaces or struts, enabling strain measurement inside complex AM build shapes. The present study is intended to establish a materials integration framework for embedded sensing architectures rather than to demonstrate immediate qualification for safety-critical aerospace or automotive applications. The Ti-6Al-4V powder layer acts as a transient thermal shield during LPBF and is not retained as a permanent porous cavity in the final component. Embedded sensing was pursued because it enables monitoring of internal strain states and subsurface load transfer that cannot be accessed reliably using surface-mounted sensors with external encapsulation.

The interplay of nozzle precision and thermal protection was further tested across four strain gauge configurations: commercial foil with PI backing, DIW-printed serpentine gauges with PI backing, glass fiber (GF) -reinforced phenolic backing, and the TPGDA backing (Fig. 3ei–ii). PI-backed gauges failed during the LPBF embedding process. Although a precise failure mechanism was not directly investigated. The observed reduction in resistance after printing is likely associated with thermally induced post-processing effects, including additional sintering of the silver nanoparticle network, while thermal expansion mismatch between the dielectric and conductive layers may also contribute to residual interfacial stresses. In comparison to GF-reinforced phenolic and TPGDA-backed gauges, which survived, demonstrating that material selection shows post-embedding success. Although PI is known for its high thermal stability[38,39] compared to many other polymers[40], failures in this case are likely to do with the LPBF processing conditions rather than the thermal limit of the material. The rapid heating and cooling cycles, steep thermal gradients, and localized energy input during the process could result in interfacial stresses and degradation of the adhesive layer bonding the gauge to the substrate, which could result in delamination.

Measurements before and after embedding showed resistance decreases ($\Delta R = 134\ \Omega$ for phenolic, $\Delta R = 144\ \Omega$ for TPGDA), consistent with additional sintering of the silver nanoparticle ink induced by residual thermal exposure. These results confirm that, when printing resolution, thermal shielding, and backing material are carefully tuned, functional strain gauges can be reliably integrated into metal parts (Fig. 3e). The observed reduction in resistance after printing is attributed to thermally induced post-processing effects, including additional sintering of the silver nanoparticle network, while thermal expansion mismatch between the dielectric and conductive layers may introduce residual interfacial stresses.

Together, these findings reveal a pathway from nozzle design to sensor survival: precise nozzle tips enable accurate deposition, the powder layer protects against LPBF thermal effects, and appropriate backing materials preserve electrical and structural integrity. This integrated approach provides a practical framework for embedding high-resolution, durable sensors in metal components fabricated via LPBF, highlighting the critical interactions between printing parameters, thermal management, and material choice. Collectively, this establishes a design framework for integrating functional sensing architectures within AM metals, linking processing parameters to device survival and performance. Although thinner powder layers may also reduce thermal exposure, a 1 mm layer was selected here to maximize process robustness and ensure reliable protection against local variations in powder packing and laser-induced heating.

Integrated fabrication and performance of embedded strain gauges

The embedded strain gauges demonstrated both cytocompatibility and functional integrity when integrated into LPBF-fabricated Ti-6Al-4V parts, highlighting their potential for biomedical and structural sensing applications. Four types of strain gauges, DIW-printed sensors with TPGDA, PI, and GF-reinforced phenolic backings, and commercial foil sensors were evaluated for biocompatibility by immersing them in PBS for three days and three weeks. Although the sensor was encapsulated within the Ti-6Al-4V structure, this assessment was performed to determine whether any leaching of components from the embedded multilayer sensor system (e.g., dielectric layers or conductive materials) could affect cell viability.

High cell viability (80–90%) was observed across all sensors (Fig. 4a), with predominantly elongated, healthy fibroblast cells confirmed by fluorescence imaging (Fig. 4b and Supplementary Fig. 6). The Ti-6Al-4V base layer, dielectric layers (TPGDA, PI, GF-reinforced phenolic), and sensor layers (TPM silver nanoparticle ink or constantan alloy) collectively exhibited minimal cytotoxicity, consistent with prior reports[41–43]. These results indicate that the multilayer sensor constructs are potentially suitable for in vivo applications, though additional long-term biocompatibility studies would be required for clinical use. Although the embedded sensors retained cytocompatibility following LPBF integration, further studies will be required to evaluate potential LPBF-induced chemical changes, ion release, and long-term biological responses in fully integrated components. Strain serves as a key indicator of implant mechanical integrity, providing insight into load transfer, deformation, and potential failure mechanisms such as loosening or stress shielding. Embedded strain sensing enables direct measurement within the load-bearing structure, offering a more representative assessment of internal mechanical conditions compared to surface-mounted sensing approaches.

Mechanical testing under three-point bending (Fig. 4c) revealed that the GF-reinforced phenolic and TPGDA-backed sensors exhibited stable strain-sensing behavior under the testing conditions (Fig. 4d, e). In contrast, the PI-backed and commercial foil sensors exhibited performance instability that is consistent with possible thermal and interfacial degradation during the LPBF process, although the underlying failure mechanism was not directly verified in the present study. For the surviving GF-reinforced phenolic and TPGDA-backed sensors, the gauge factors (K) increased substantially after embedding, likely due to localized thermally induced sintering of the TPM silver nanoparticle ink, which improved electrical connectivity within the conductive network. The embedded strain gauge was positioned on the tensile surface of the specimen and located at the mid-span region directly beneath the loading nose to capture maximum tensile strain during three-point bending. For the surviving sensor configurations, the increase in gauge factor was substantial, rising from 1.89 to 4.26 for the GF-reinforced phenolic-backed sensor and from 1.84 to 4.52 for the TPGDA-backed sensor following embedding (Fig. 4d), corresponding to increases of approximately 125% and 146%, respectively. This demonstrates that the LPBF process can embed DIW-printed sensors while inducing partial curing, a slight densification of the conductive ink that improves electrical connectivity without complete degradation of the dielectric or backing layer (Fig. 4di–iv). This demonstrates that the LPBF process can both embed and partially cure DIW-printed sensors without complete degradation. The GF-reinforced phenolic and TPGDA-backed sensors survived the embedding process, while PI-backed and commercial foil

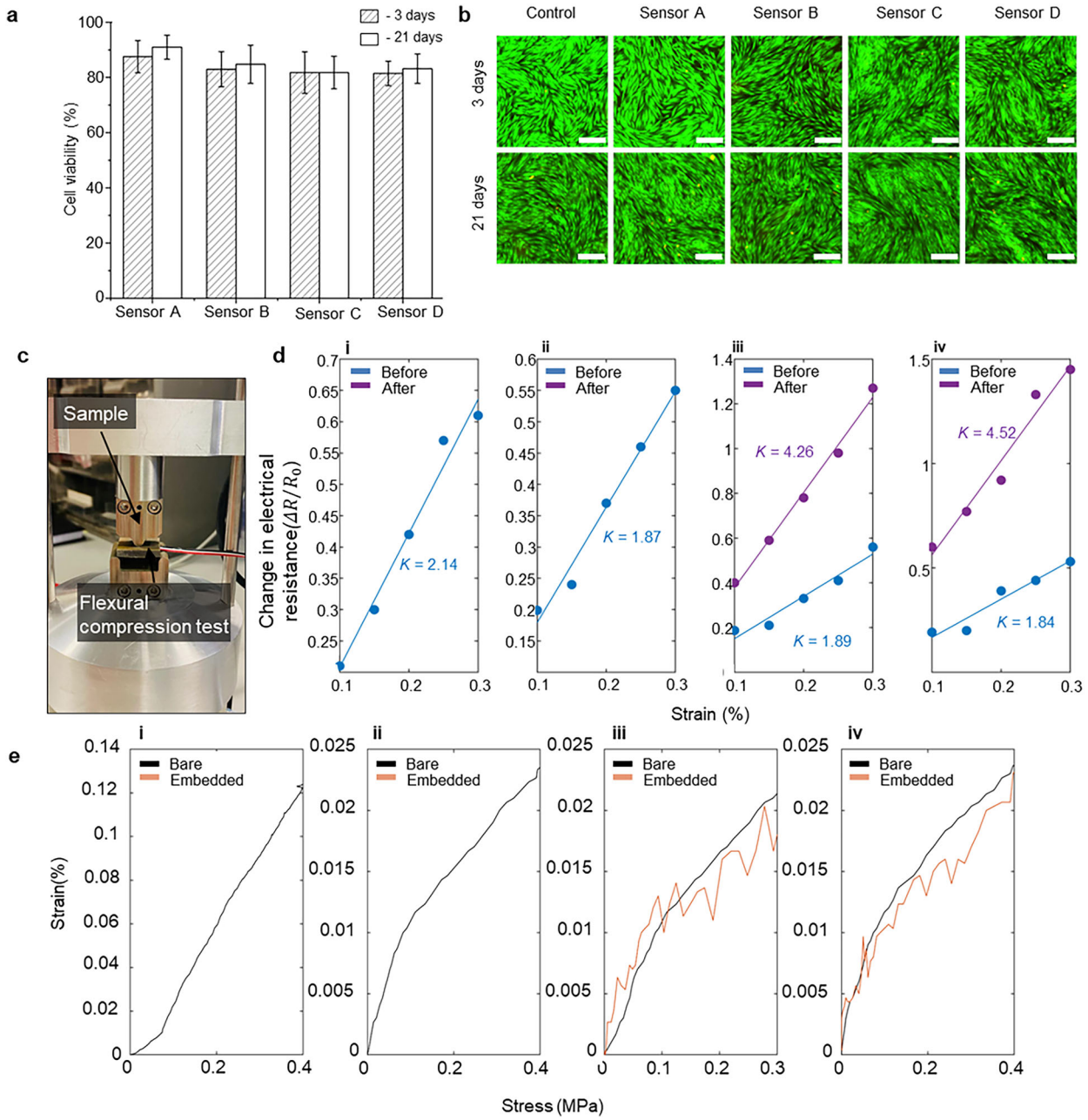

Fig. 4 | Cytotoxicity test for four sensors (strain gauges). Sensor A, which is a hybrid layer sensor with a Ti-6AI-4V base layer, tripropylene glycol diacrylate (TPGDA) dielectric layer, and a sensor layer printed with 50 wt. % dispersion in tripropylene glycol monomethyl ether (TPM) silver nanoparticle ink. Sensor B is a polyamide film (PI) dielectric layer and a sensor layer printed with TMP silver nanoparticle ink. Sensor C is a glass fiber (GF) reinforced phenolic dielectric layer and a sensor layer printed with TMP silver nanoparticle ink. Sensor D is a commercial foil gauge sensor that has a PI backing. **a** (3-(4,5-Dimethylthiazol-2-yl)-2,5-diphenyltetrazolium bromide) MTT assay showing cell viability of human dermal fibroblast (HDF) cell lines of the four strain gauges (sensor A, B, C, and D) that were soaked in phosphate-buffered saline (PBS) for 3 and 21 days (including controls). **b** Fluorescence microscopy images of HDF cells were immersed with the four-strain gauge after 72 hours of incubation (see Supplementary Fig. 6). All scale bars are 1050 μm. Validation of the sensor embedding process, strain gauge sensor operation with comparison to bare strain gauges, where bare strain gauges refer to the same devices prior to LPBF embedding. **c** Mechanical testing set-up for monitoring of in situ strain gauges of the Ti-6AI-4V embedded parts. **d** Change of resistance divided by initial resistance against strain, where the gradient is the gauge factor (K) stress-strain profile for the sensor comparing the bare strain gauges to the embedded strain gauges, which include **ei** a commercial foil strain gauge with a PI backing, **eii** direct ink write (DIW) printed strain gauge with 50 wt. % dispersion in tripropylene glycol TPM silver nanoparticle ink with a PI backing, **eiii** DIW-printed strain gauge with 50 wt. % dispersion in TPM silver nanoparticle ink with GF reinforced phenolic backing, and **eiv** a Ti-6AI-4V base layer, TPGDA backing, and a sensor layer printed with 50 wt. % dispersion in TPM silver nanoparticle ink. **a** Cell viability data are presented as mean ± standard deviation from triplicate measurements ($n = 3$ technical replicates). Mechanical strain-sensing data shown in (**d**, **e**) are representative results from a single specimen for each sensor configuration ($n = 1$).

sensors were prone to thermal-induced performance variations. Some fluctuations in the stress-strain curves were observed for the surviving sensors, likely due to laser-induced thermal effects causing minor resistance changes and Wheatstone bridge imbalance (Fig. 4ei–iv). The overall stress-strain response was preserved, confirming the feasibility of embedding functional strain gauges using a powder shielding approach.

These results establish a linked framework for integrating functional, biocompatible strain gauges into LPBF-fabricated metal parts. High cell

viability demonstrates suitability for biomedical applications, while mechanical testing confirms that thermal protection via powder layers and appropriate backing materials preserves strain-sensing performance. Optimizing nozzle geometry, powder thickness, and backing material selection collectively ensures that embedded sensors maintain both biological safety and functional integrity, providing a robust strategy for next-generation smart implants and structural monitoring devices. Together, these findings indicate that careful selection of powder thickness, backing material, and sensor design allows embedded sensors to maintain both functional integrity and cytocompatibility, providing a methodology for next-generation smart implants and structural monitoring devices. More broadly, they establish design criteria linking backing material, thermal exposure, and interfacial stability, providing a framework for embedding multifunctional devices within structural metals for biomedical and sensing applications. These results support the cytocompatibility of the embedded sensor material system under the conditions tested, while further long-term biological evaluation will be required to assess suitability for clinical implantation. The mechanical testing reported here was conducted within the elastic regime to assess strain transfer and sensing functionality following LPBF embedding. Evaluation of fracture behavior and long-term cyclic durability remains the subject of future work. The mechanical testing results presented here are based on representative specimens for each sensor configuration and are intended to demonstrate proof-of-concept strain-sensing functionality following LPBF embedding. The same sensor was characterized before and after embedding to directly assess the influence of the embedding process on sensing performance. As additively manufactured sensors may exhibit specimen-to-specimen variability arising from manufacturing tolerances and process limitations, individual calibration and gauge-factor determination may be required for practical deployment. Future studies should include replicate specimens and statistical analysis to assess reproducibility and quantify variability in sensor performance. The strain-sensing performance reported here was evaluated under controlled room-temperature conditions; for applications involving variable thermal environments, temperature compensation and thermal-cycling stability will require further investigation. Interfacial integrity was not quantified by dedicated adhesion or delamination testing in the present study; therefore, conclusions are based on indirect evidence from sensor survival and retained functionality. Future work should assess interfacial reliability under cyclic thermo-mechanical loading. The mechanical strain-sensing results presented for each sensor configuration were obtained from a single representative specimen ($n = 1$) to demonstrate proof of concept functionality following LPBF embedding.

Methods

Figure 5 shows a flow chart that summarizes the sensor embedding methodology. Figure 5 a shows four types of strain gauges that were embedded using LPBF, each consisting of a dielectric backing and a sensing layer: (1) a commercial foil gauge on a PI backing, (2) a DIW-printed gauge with commercial PI, (3) a DIW-printed gauge with GF-reinforced phenolic, and (4) a DIW-printed gauge with a thin-film TPGDA dielectric deposited on a moving substrate in a R2R facility. The sensing layer for the DIW-printed gauges was deposited using TPM silver nanoparticle ink. Full material specifications, particle sizes, and supplier details are provided in the Supplementary. Commercial and DIW gauges with PI or GF-reinforced phenolic backings were bonded to Ti-6Al-4V substrates using adhesive. For TPGDA thin films, R2R deposition and roller compression were used to achieve adhesion. Deposition rates, curing conditions, and roller parameters are outlined in the Supplementary Methods and Supplementary Fig. 7. The off-line R2R thin-film deposition approach was selected to enable controlled fabrication of uniform dielectric layers prior to LPBF integration, while surface activation treatments were used to enhance adhesion between the dielectric layer and the Ti-6Al-4V substrate.

LPBF was used to embed the sensors within Ti-6Al-4V. Samples were printed under an argon atmosphere using an Aconity Lab system with optimized process parameters. A laser power of 190 W and scan speed of 1.2 m/s were maintained throughout the build. The full process map, hatching strategy, and powder specifications are provided in Supplementary Tables 6–8. The chosen fabrication sequence was selected to ensure compatibility between the R2R/DIW sensor fabrication stages and the LPBF process. Direct fabrication of the sensing architecture within a partially completed LPBF build would require interruption of the build process and expose the sensor to additional recoating and laser-processing stages, increasing the risk of mechanical and thermal damage prior to encapsulation.

Strain gauge designs were printed onto dielectric layers via DIW, using custom nozzles and a controlled translational stage. Sensors were cured by thermal sintering between 100 and 250 °C. Details of nozzle manufacturing, scanning electron microscopy (SEM) imaging, printing speeds, and curing times are provided in Supplementary Table 5 and Supplementary Fig. 4. Surface and material characterization were carried out by AFM, FTIR, DSC, TGA, and contact angle measurements to assess dielectric properties and printability. Instrument models, acquisition parameters, calibration details, and Supplementary Figs. (Supplementary Methods) Provide full characterization protocols. For wiring, a thermally conductive epoxy (MG Chemicals 8329TCS) was used for bonding and electrical/mechanical stabilization of sensor connections. The present wiring configuration requires local access to the sensor contact pads and therefore does not yet represent a fully enclosed near-net-shape implementation. Future embedded architectures may incorporate conductive feedthroughs, interconnect channels, or integrated connectors to enable full encapsulation. Two embedding strategies were used: (1) cold embedding with powder protection for PI and phenolic-based sensors, and (2) a hybrid process combining R2R and DIW for TPGDA-based sensors. Schematics of both workflows are summarized by Fig. 5b–e. Stepwise embedding protocols are provided in Supplementary Fig. 7 and Fig. 5d. Thermal simulations were performed in Abaqus to analyze heat transfer through the 1 mm protective powder layer. Mesh details, Goldak's model parameters[44], and material constants are summarized in Supplementary Tables 6–8 and Supplementary Fig. 5.

Mechanical performance was validated using three-point bending tests, while biocompatibility was assessed on human dermal fibroblasts (HDF) cell lines using LIVE/DEAD and 3-(4,5-dimethylthiazol-2-yl)-2,5-diphenyltetrazolium bromide (MTT) assays. Complete assay protocols, incubation conditions, and statistical analyses are detailed in Supplementary Methods and Supplementary Fig. 6. Strain signals from embedded gauges were recorded using a Wheatstone bridge circuit connected to an Arduino-based wireless data acquisition system shown in Fig. 5d. Circuit diagrams, component specifications, and software versions are shown in Supplementary Fig. 8.

Conclusions

We have demonstrated a strategy for creating multifunctional titanium by embedding strain-sensing architectures directly within Ti-6Al-4V during LPBF. By combining direct printing of multilayer polymer–metal gauges with a Ti-6Al-4V powder layer for thermal protection, we show that thermally sensitive sensing elements can survive incorporation into a high-temperature metal AM process. Among the architecture evaluated, TPGDA- and GF phenolic-backed printed sensors retained electrical functionality and strain-sensing performance after embedding, whereas polyimide-based configurations were more susceptible to thermal and interfacial failure. Rather than presenting single device optimization, this study establishes a materials integration framework linking dielectric surface properties, conductive ink curing behavior, backing-layer selection, and powder-mediated thermal shielding to the successful embedding of functional sensors in LPBF titanium. Although TPGDA and TPM silver nanoparticle ink were used here as model materials, the design principles identified, namely control of dielectric surface chemistry and morphology, management of curing-temperature limits, and use of powder-mediated thermal shielding, are expected to be transferable to other printable polymer–metal sensor systems. Although the present study focuses on demonstrating feasibility, several stages of the workflow are compatible with

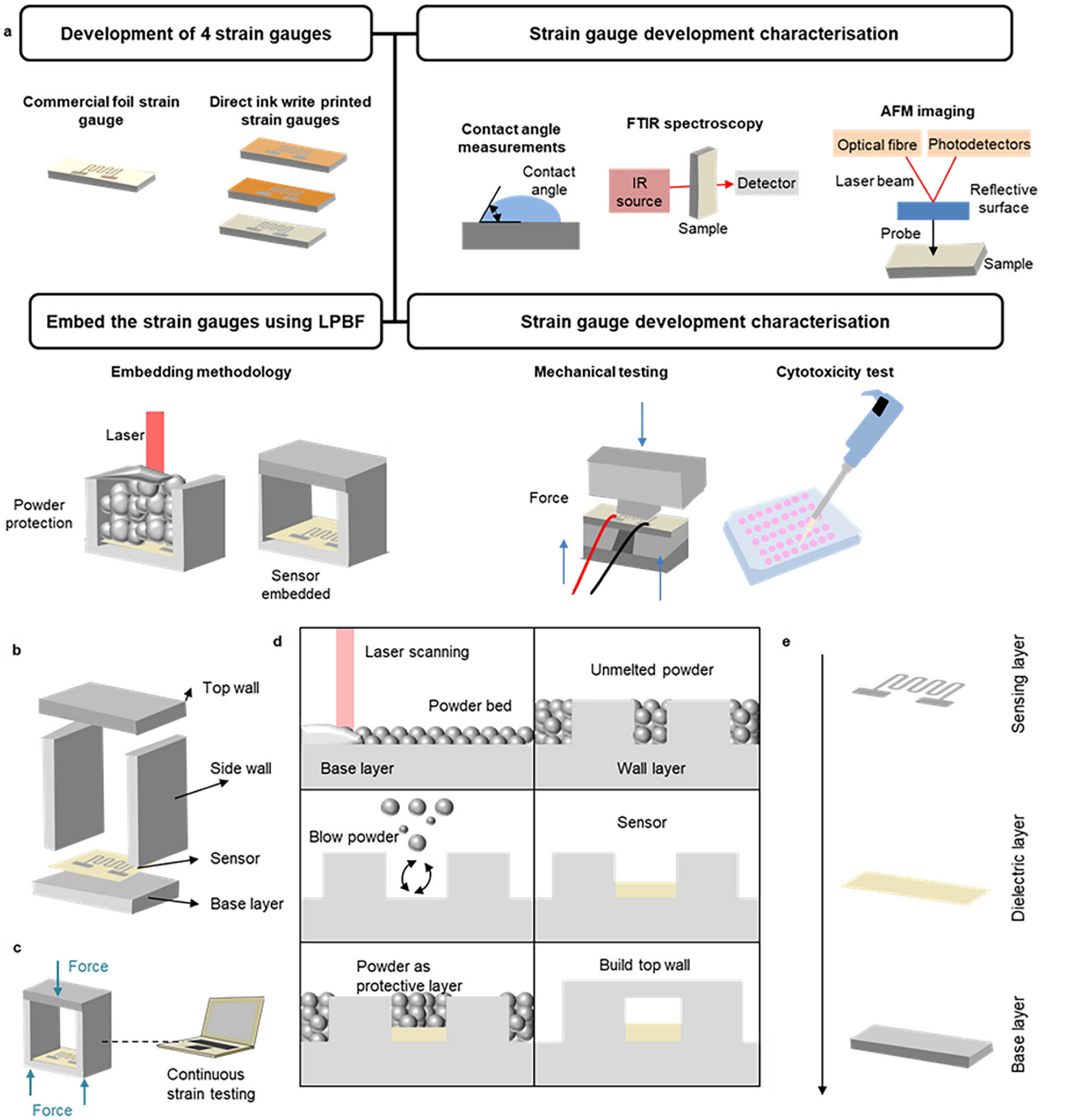

Fig. 5 | a A flow diagram describing the stages to achieve the sensor embedding process which includes (1) development of the four strain gauges that include a commercial foil gauge on a polyamide (PI) backing, a direct ink write (DIW) printed gauge with commercial PI, a DIW-printed gauge with glass fiber (GF) reinforced phenolic, and a DIW-printed gauge with a thin-film tripropylene glycol diacrylate (TPGDA) dielectric deposited by roll-to-roll (R2R). (2) Strain gauges are characterized to analyze the wettability through contact angle measurements, Fourier transform infrared (FTIR) spectroscopy, and atomic force microscopy (AFM). (3) Embedding stage, where the four strain gauges were embedded in the Ti-Al-4V component using laser powder bed fusion (LPBF). (4) The embedded and non-embedded strain gauges were evaluated to analyze the effect of embedding. **b** A schematic of the strain gauges embedded, which consists of a base layer, a strain gauge, which is deposited on the base layer, and encapsulated in a cavity-like structure. **c** Once the gauges are embedded, the embedded samples are tested using mechanical testing, where continuous strain measurements are taken, as shown by the schematic. **d** A schematic of the embedding process where powder is used as a protective layer to protect the sensor when the laser is scanning over the sensor to print the top wall. **e** A schematic summarizing the three core components, sensor embedding layers, which includes the base layer, which is made of Ti-6Al-4V, the dielectric layer, which is the barrier layer between the base layer and conductive layer, and is composed of a polymer, and the sensing layer, which is a conductive layer that is composed of a silver conductive nanoparticle ink.

industrial scale-up. R2R dielectric deposition and plasma surface treatment are inherently high-throughput processes, while automated multi-nozzle printing approaches could enable scalable fabrication of the sensing architectures in future implementations.

These results show that metal AM can be extended beyond structural fabrication to produce titanium components with built-in sensing capability. More broadly, the work establishes a materials-integration framework in which interfacial design, curing conditions, and powder-mediated

thermal shielding are jointly used to incorporate functional devices into structural metals. This approach provides a foundation for self-monitoring metallic systems in aerospace, biomedical, and intelligent manufacturing applications. Future work should focus on broadening the range of compatible dielectric and conductive materials, improving long-term reliability and cyclic stability, and extending the strategy to other sensing modalities and metal AM platforms. These findings are relevant to application areas including aerospace structures, biomedical devices, and intelligent manufacturing, although further domain-specific validation will be required for end-use deployment.

Data availability

Representative sample data is summarized in the figures (and supplementary data). Additional datasets generated and analyzed during the study are available upon reasonable request through the corresponding authors due to the large size and volume of data acquired.

Received: 26 March 2026; Accepted: 18 August 2026;
Published online: 09 September 2026

References

1. Hegazy, M. A., Nada, N., Elhaes, H., Ibrahim, M. A. & Ezzat, H. A. Advanced polymer-based humidity sensor for aerospace applications implementing ZnO-G: theoretical and experimental study. *Sci. Rep*. **16**, 6339 (2026).
2. Tian, X. et al. Implant-to-implant wireless networking with metamaterial textiles. *Nat. Commun*. **14**, 4335 (2023).
3. Wu, Y. et al. An overview of 3D printed metal implants in orthopedic applications: present and future perspectives. *Heliyon* https://doi.org/10.1016/j.heliyon.2023.e17718 (2023).
4. Kim, M.-J., Lasalde-Ramírez, J. A., Heng, W. & Gao, W. Biomolecular profiling for noninvasive health monitoring. *Nat. Biotechnol*. https://doi.org/10.1038/s41587-026-03050-2 (2026).
5. Albero Blanquer, L. et al. Optical sensors for operando stress monitoring in lithium-based batteries containing solid-state or liquid electrolytes. *Nat. Commun*. **13**, 1153 (2022).
6. Yuan, F. et al. Tailorable biosensors for real-time monitoring of stress distribution in soft biomaterials and living tissues. *Nat. Commun.* **16**, 1081 (2025).
7. Zhang, Y. et al. Localizing strain via micro-cage structure for stretchable pressure sensor arrays with ultralow spatial crosstalk. *Nat. Commun*. **14**, 1252 (2023).
8. Rogers, J. A., Someya, T. & Huang, Y. Materials and mechanics for stretchable electronics. *Science* **327**, 1603–1607 (2010).
9. Jriyasetapong, K. et al. mRNA encoding bone morphogenetic protein-2 facilitated peri-implant bone formation of titanium implants placed in rat femurs. *Sci. Rep*. **15**, 17852 (2025).
10. Peng, H. et al. Achieving high strain hardening and strength in an additively manufactured titanium alloy. *Nat. Commun.* **16**, 10224 (2025).
11. Banerjee, D. & Williams, J. C. Perspectives on titanium science and technology. *Acta Mater.* **61**, 844–879 (2013).
12. Lee, J. A. et al. Active learning framework to optimize process parameters for additive-manufactured Ti-6Al-4V with high strength and ductility. *Nat. Commun.* **16**, 931 (2025).
13. Wang, X. et al. A rubber-based sensor with over 100 million-level ultra-sensitivity (0–10% strain range) via 3D super-interface. *Nat. Commun*. https://doi.org/10.1038/s41467-026-70434-y (2026).
14. Rahman, S. et al. Additively manufactured smart metallic structures with embedded sensing: a review. *Prog. Addit. Manuf.* https://doi.org/10.1007/s40964-025-01481-y (2026).
15. Mann, S. et al. Connected, digitalized wire arc additive manufacturing: utilizing data in the internet of production to enable industrie 4.0. *Sci. Rep*. **15**, 38672 (2025).
16. Martin, A. A. et al. Dynamics of pore formation during laser powder bed fusion additive manufacturing. *Nat. Commun*. **10**, 1987 (2019).
17. Zhong, H. Z. et al. Laser powder bed fusion of complex metal lattice metamaterials: a structurally robust holistic design approach. *NPJ Adv. Manuf.* **2**, 9 (2025).
18. Gao, S. et al. Additive manufacturing of alloys with programmable microstructure and properties. *Nat. Commun*. **14**, 6752 (2023).
19. Jung, I. D. et al. Embedding sensors using selective laser melting for self-cognitive metal parts. *Addit. Manuf*. **33**, 101151 (2020).
20. Stoll, P., Gasparin, E., Spierings, A. & Wegener, K. Embedding eddy current sensors into LPBF components for structural health monitoring. *Prog. Addit. Manuf.* **6**, 445–453 (2021).
21. Ahmed, F., Forhad, M. S. & Porag, M. H. Spectral behavior of fiber Bragg gratings during embedding in 3D-printed metal tensile coupons and cyclic loading. *Sensors* **24**, 3919 (2024).
22. Bareth, T., Fromm, N., Lehmann, M., Schlick, G. & Seidel, C. A methodical approach for the integration of foil-type strain gauges in PBF-LB/M components. *Prog. Addit. Manuf.* **10**, 3963–3976 (2025).
23. Li, W. et al. Highly customizable, ultrawide-temperature free-form flexible sensing electronic systems based on medium-entropy alloy paintings. *Nat. Commun.* **16**, 7351 (2025).
24. Smith, B. N. et al. Capillary flow printing of submicrometre carbon nanotube transistors. *Nat. Electron.* **8**, 1027–1037 (2025).
25. Abbas, G. A. et al. A high-yielding evaporation-based process for organic transistors based on the semiconductor DNTT. *Org. Electron.* **15**, 1998–2006 (2014).
26. He, Y. et al. A tripropylene glycol diacrylate-based polymeric support ink for material jetting. *Addit. Manuf.* **16**, 153–161 (2017).
27. Khan, Z. et al. Iterative printing of bulk metal and polymer for additive manufacturing of multi-layer electronic circuits. *NPJ Adv. Manuf.* **1**, 1 (2024).
28. Guo, Z., Yu, P., Liu, Y. & Zhao, J. High-precision resistance strain sensors of multilayer composite structure via direct ink writing: optimized layer flatness and interfacial strength. *Compos. Sci. Technol*. **201**, 108530 (2021).
29. Feldhausen, T. et al. Embedding ceramic components in metal structures with hybrid directed energy deposition. *Int. J. Adv. Manuf. Technol.* **125**, 4425–4433 (2023).
30. Binder, M. et al. Additive manufacturing of a passive, sensor-monitored 16MnCr5 steel gear incorporating a wireless signal transmission system. *Procedia CIRP* **107**, 505–510 (2022).
31. Maleki, H. & Bertola, V. Recent advances and prospects of inkjet printing in heterogeneous catalysis. *Catal. Sci. Technol.* **10**, 3140–3159 https://doi.org/10.1039/d0cy00040j (2020).
32. Belser, R. B. & Hicklin, W. H. Temperature coefficients of resistance of metallic films in the temperature range 25°to 600 °C. *J. Appl. Phys.* **30**, 313–322 (1959).
33. Kim, Y., Kim, Y., Lee, C. & Kwon, S. Thin polysilicon gauge for strain measurement of structural elements. *IEEE Sens. J.* **10**, 1320–1327 (2010).
34. Kalpana, H. M. & Siddeswara Prasad, V. Development of the invar36 thin film strain gauge sensor for strain measurement. *Meas. Sci. Technol*. **25**, 065102 (2014).
35. Ajovalasit, A., D'Acquisto, L., Fragapane, S. & Zuccarello, B. Stiffness and reinforcement effect of electrical resistance strain gauges. *Strain* **43**, 299–305 (2007).
36. Wei, C. et al. Easy-to-operate fabrication of tapered glass capillaries for microdroplet generation. *J. Micromech. Microeng.* **29**, 0–9 (2019).
37. Bergman, T. L. & Levine, A. S. *Fundamentals of Heat and Mass Transfer* (John Wiley & Sons, Inc., 2019).
38. Torrecillas, R., Baudry, A., Dufay, J. & Mortaigne, B. Thermal degradation of high performance polymers—influence of structure on polyimide thermostability. *Polym. Degrad. Stab.* **54**, 267–274 (1996).
39. Celia, J. A. Degradation and stability of polyimides. *Polym. Degrad. and Stab.* **36**, 99–110 (1992).

40. Benedito, M., Manca, F. & Palla, P. L. Rate-dependent force-extension models for single-molecule force spectroscopy experiments. *Polym. Biol.* **17**, 056002 (2020).
41. Wang, M., Lai, X., Shao, L. & Li, L. Evaluation of immunoresponses and cytotoxicity from skin exposure to metallic nanoparticles. *Int. J. Nanomed.* **13**, 4445–4459 (2018).
42. Kessler, A., Reichl, F. X., Folwaczny, M. & Högg, C. Monomer release from surgical guide resins manufactured with different 3D printing devices. *Dent. Mater.* **36**, 1486–1492 (2020).
43. McKinnon, K. M. Flow cytometry: an overview. *Curr. Protoc. Immunol.* **120**, 5.1.1–5.1.11 (2018).
44. Yang, Y., Zhou, X., Li, Q. & Ayas, C. A computationally efficient thermo-mechanical model for wire arc additive manufacturing. *Addit. Manuf*. **46**, 102090 (2021).
45. Bhatt, A. et al. In situ characterisation of surface roughness and its amplification during multilayer single-track laser powder bed fusion additive manufacturing. *Addit. Manuf*. **77**, 103809 (2023).

Acknowledgements

The Deben CT500 was provided by The University of Manchester at Harwell (UoMaH). Thanking Aikta Sharma, Ratul Kumar Biswas, Er Wanjau Muriithi, Jingwen Liu, Matas Petreikis, Ching-Mei, Priya Gupta, Biswajoy Bacgchi, Vikaramjeet Singh, Temitope Odedeyi, Joseph Hadden, Mary Ryan, Phillip Stanley-Marbell, and James.T Meech for their assistance and advice throughout the project.

Author contributions

A.B.: conceptualization, methodology, formal analysis, investigation, writing—original draft, and visualization. W.C.: conceptualization, methodology, and investigation. Z.W.: conceptualization, methodology, investigation, data curation, and writing—review and editing. P.K.: methodology, investigation, data curation, and writing—review and editing. P.B.: methodology and investigation. Samy Hocine: methodology. E.R.: methodology. H.A.: supervision, conceptualization, resources, investigation, and writing—review and editing, funding acquisition. Rob Snell: methodology and investigation. I.T.: supervision, conceptualization, resources, writing—review and editing, and funding acquisition. P.D.L.: supervision, conceptualization, resources, investigation, writing—review and editing, and funding acquisition. M.K.T.: supervision, conceptualization, resources, investigation, writing—review and editing, and funding acquisition. P.D.L., M.K.T., and A.B. conceived the research/project. A.B., W.C., and Z.W. designed the experiments. A.B., Z.W., P.K., and W.C. performed data analysis and interpretation of the results. A.B., M.K.T., and P.D.L. led the interpretation of the results and writing of the manuscript. W.C. and A.B. performed cytotoxicity analysis. P.K. and A.B. performed contact angle tests. Z.W. and H.A. performed the TPGDA experiments, and A.B. analyzed the results. A.B. and P.B. designed the microcontroller with assistance from PK. A.B. performed the computational analysis with assistance from E.R. and S.H. The embedding of the sensor was performed by A.B., R.S., and I.T.

Funding

The authors acknowledge financial support from the EPSRC MAPP Future Manufacturing, Hub (EP/P006566/1, www.mapp.ac.uk); the UK-EPSRC (grants EP/W031167/1, EP/W032147/1, EP/W037483/1, EP/W006774/1, EP/W003333/1, and EP/V061798/1); the Royal Academy of Engineering (CiET1819/10); and the UKRI - Research Complex at Harwell for use of facilities. RS acknowledges the Henry Royce Institute for Advanced Materials, funded through EPSRC grants EP/R0066X/1, EP/S019367/1, EP/P02470X/1, and EP/PO25285/1. This work was partially supported by the Wellcome/EPSRC Centre for Interventional and Surgical Sciences (WEISS) (203145/16/Z).

Competing interests

The authors declare no competing interests.

Additional information

Supplementary information The online version contains supplementary material available at https://doi.org/10.1038/s43246-026-01346-z.

Correspondence and requests for materials should be addressed to Alisha Bhatt, Peter D. Lee or Manish K. Tiwari.

Peer review information *Communications Materials* thanks Im Doo Jung, Semih Akin and the other, anonymous, reviewer(s) for their contribution to the peer review of this work. A peer review file is available.